New insights from three-phase fractional-flow modeling of foam-oil displacements in porous media

Tang, Jinyu; Castañeda, Pablo; Marchesin, Dan; Rossen, William R.

DOI
10.1016/j.geoen.2025.214091

Publication date
2025

Document Version
Final published version

Published in
Geoenergy Science and Engineering

255 (2025) 214091

Contents lists available at ScienceDirect

Geoenergy Science and Engineering

journal homepage: www.sciencedirect.com/journal/geoenergy-science-and-engineering

New insights from three-phase fractional-flow modeling of foam-oil displacements in porous media

Jinyu Tang [a,*], Pablo Castañeda [b,c], Dan Marchesin [d], William R. Rossen [e]

[a] Department of Chemical and Petroleum Engineering, United Arab Emirates University, Al Ain, Abu Dhabi, 15551, United Arab Emirates
[b] Departamento Académico de Matemáticas, Instituto Tecnológico Autónomo de México (ITAM), Río Hondo 1, 01080, CdMx, Mexico
[c] Instituto de Matemáticas, Universidad Nacional Autónoma de México (UNAM), Circuito Exterior s/n, Ciudad Universitaria, 04510, CdMx, Mexico
[d] National Institute of Pure and Applied Mathematics (IMPA), Estrada Dona Castorina, 110, Rio de Janeiro, RJ, 22460-320, Brazil
[e] Department of Geoscience and Engineering, Delft University of Technology, Delft, 2628 CN, the Netherlands

ARTICLE INFO

Keywords:
Gas sweep efficiency
Foam mobility control
Foam-oil interactions
Oil-bank creation
Foam propagation
Three-phase fractional-flow modeling

ABSTRACT

For the first time, we apply three-phase fractional-flow theory combined with the wave-curve method to better understand the mechanisms of foam displacements with oil in porous media, employing a widely used foam model. Fractional-flow theory demonstrates that oil saturation in foam-created oil banks never exceeds the upper limit for stable foam, *fmoil* (i.e. an oil saturation above which foam is killed); see (Tang et al., 2019c) and section 3.4 below. This constraint suggests a criterion for creating significant oil banks: for the surfactant formulation, *fmoil* must be far above the initial oil saturation. We identify key factors controlling foam and oil-bank propagation: *fmoil*, foam quality, the regime in which foam is injected and foam strength at both injection and initial states. The mechanisms of these factors are revealed through a material balance on gas: any factor increasing gas volume injected while maintaining adequate foam strength, or reducing gas saturation in the foam region, accelerates foam propagation, and vice versa. Also, an optimal foam injection strategy is identified: inject foam in the low-quality regime near the transition foam quality (Tang et al., 2019a, 2019b), at which mobility reduction is at its maximum. This rule's universality needs to be further verified. Fractional-flow solutions, free of numerical artifacts, can be used to benchmark numerical simulators and machine-learning approaches for foam processes.

1. Introduction

Carbon dioxide (CO_2) injection into geological formations is a crucial means for enhanced oil recovery (EOR) and carbon sequestration. Nevertheless, its potential is limited by the poor sweep and trapping efficiency of gas injected, due to gas fingering arising from its high mobility, gas channeling resulting from formation heterogeneity and gravity override caused by gas/liquid density contrast (Glass and Yarrington, 2003; Reynolds and Krevor, 2015). Foam produces remarkable reductions in gas mobility, e.g. by an order of 10–10^4 (Schramm and Joan, 1994; Rossen, 1996). This feature gives foam broad subsurface applications: EOR in the oil industry (Rossen, 1996; Kovscek et al., 1995; Lake et al., 2014); acid diversion in well stimulation (Thompson and Gdanski, 1993; Zhou and Rossen, 1995); removal of non-aqueous-phase liquid (NAPL) contaminants in soil and aquifer remediation (Estrada et al., 2015; Bertin et al., 2017); and carbon sequestration (Bui et al., 2018; Castaneda-Herrera et al., 2018; Rossen et al., 2024; Wu et al., 2024). Fundamentally, foam benefits EOR and carbon sequestration via two mechanisms: improved gas sweep and increased gas saturation in the swept zone (Rossen et al., 2024). Improved sweep enhances oil recovery and opens additional pore space for CO_2 storage. Increased gas saturation in the foam swept zone further increases the amount of CO_2 stored.

Understanding the physics of foam flow with oil is especially crucial for accurate modeling and evaluation of foam EOR for carbon-sequestration processes in the field. This has been a long-standing challenge given the complex interactions between foam and oil (Farajzadeh et al., 2012). Foam shows the existence of two flow regimes in porous media that depend on foam quality, f_g (i.e. volume fraction of gas in foam) (Osterloh and Jante, 1992): the high- and low-quality

This article is part of a special issue entitled: Reservoir Sweep Efficiency Improvement published in Geoenergy Science and Engineering.

* Corresponding author.
E-mail address: j.tang@uaeu.ac.ae (J. Tang).

https://doi.org/10.1016/j.geoen.2025.214091
Received 28 January 2025; Received in revised form 2 July 2025; Accepted 17 July 2025
Available online 18 July 2025

regimes; see Fig. 1a. The upper-left, high-quality regime reflects abrupt foam collapse as water saturation falls below the limiting water saturation, named *fmdry* in the STARS simulator (Zhou and Rossen, 1995; Khatib et al., 1988). The lower-right, low-quality regime reflects the gas-mobility reduction, named *fmmob* in STARS, that applies at wetter conditions. The intersection between the two foam-flow regimes marks the transition foam quality, corresponding to maximum reduction in total mobility. A recent lab study (Tang et al., 2019a) demonstrates that the two flow regimes also apply to foam flow with oil, as shown in Fig. 1b.

A widely used model for representing foam in porous rocks is STARS (Computer Modelling Group, 2015). The suitability of the model for representing foam with and without oil has been verified by model fitting to steady-state coreflood data (Tang et al., 2019a; Alvarez et al., 2001; Kim et al., 2005). The good agreement between fitted results and data reveals foam-oil interaction. In the high-quality regime oil destabilizes foam by raising *fmdry*. In the low-quality regime, oil weakens foam by reducing *fmmob*. For the detailed procedure for fitting foam model parameters in STARS, one may refer to published studies (Cheng et al., 2000; Boeije and Rossen, 2015; Abbaszadeh et al., 2018).

The presence of foam complicates the three-phase flow problem, introducing strong non-linearity, abrupt mobility changes at the foam/no foam boundary, and ambiguous phase identification in a miscible displacement (Rossen, 2013). These complexities pose large uncertainty in numerical simulation solutions and may result in numerical artifacts. Therefore, it is necessary to have a reliable way to calibrate numerical simulators.

While it requires simplifying assumptions, fractional-flow theory is advantageous since it is free of numerical artifacts. Furthermore, the theory reveals deep insights into complex multi-phase displacements such as by foam (Charbeneau, 1988; LaForce and Johns, 2005; Rossen et al., 2011; You et al., 2015). Ashoori et al. (2010) discuss fractional-flow theory for first-contact miscible CO_2 displacements with foam. Here we focus on three-phase fractional-flow modeling of immiscible foam flooding, with the STARS model and model parameters that fit CO_2 foam data. The three-phase displacement problem with foam is solved by combining three-phase fractional-flow theory with the wave-curve method (WCM) (Azevedo et al., 2010). The fractional-flow solutions reveal useful physical insights into aspects that control the success of foam EOR for carbon sequestration processes. In particular, these insights shed light on foam stability in the oil bank (one key to foam success), criteria for creating a significant oil bank by foam, factors that control foam and thus oil-bank propagation, and the mechanisms of those factors on foam propagation.

In addition, since fractional-flow solutions are free of numerical artifacts, they can be used as benchmarks to calibrate numerical simulators or machine-learning approaches for foam EOR and carbon-sequestration processes (Lyu et al., 2021).

2. Three-phase fractional-flow modeling of foam flow with oil

2.1. Three-phase fractional-flow theory

For the purpose of this study, we have made the following simplifications: one-dimensional flow; incompressible fluids and rock; negligible gravity effects; all phases immiscible; isothermal process; no dispersive processes, e.g. diffusion, dispersion or capillary-driven flow; local equilibrium attained immediately; Newtonian rheology of all phases; uniform surfactant concentration in the aqueous phase everywhere. Currently, only upon these simplifications, one could solve for the analytical solutions of a three-phase foam-flow problem. In this initial study, a phase-behavior advantage for oil mobilization is not considered, i.e. there is no oil swelling by gas, stripping of oil into gas, or gas-oil miscibility. Mobility control is thus the key to improving sweep efficiency, which delivers gas into zones where these advantages can work in a miscible displacement.

With the simplifications above, a foam-oil flow system is governed by two independent mass-conservation equations:

$$\varphi\frac{\partial S_w}{\partial t}+u\frac{\partial f_w}{\partial x}=0, \tag{1}$$

$$\varphi\frac{\partial S_o}{\partial t}+u\frac{\partial f_o}{\partial x}=0, \tag{2}$$

where φ is porosity, S_w and S_o are water and oil saturations, x and t are position and time, and u is the total superficial velocity. f_j is the fractional flow of phase j, defined as

$$f_j\equiv\frac{u_j}{u}, \tag{3}$$

where subscript $j = w$, o or g denotes water, oil or gas. u_j is the Darcy velocity:

$$u_j=\frac{kk_{rj}}{\mu_j}|\nabla p|, \tag{4}$$

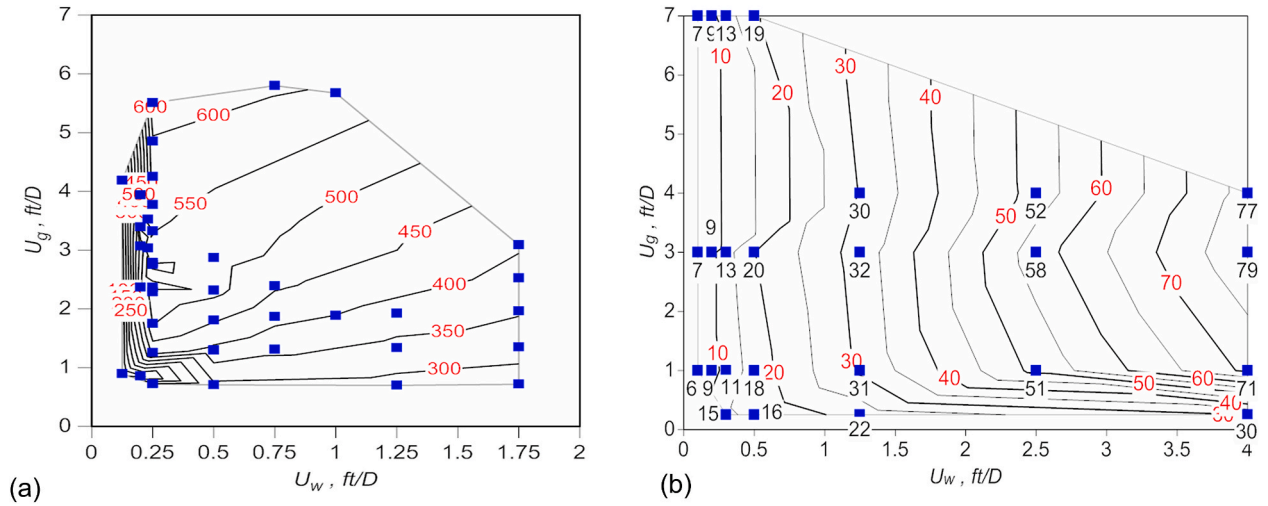

Fig. 1. Pressure gradient (psi/ft) as a function of gas (u_g) and water (u_w) superficial velocities for foam flow in Bentheimer sandstone of 1.98 Darcies (Tang et al., 2019a, 2019b): (a) without oil; (b) with oil. In the case of Fig. 1b, oil is co-injected with foam at a fixed oil/water ratio of 0.25. Upper-left and lower-right contours correspond to the high- and low-quality regimes, respectively.

where k is permeability, k_{rj}, the relative permeability, μ_j, the viscosity and $|\nabla p|$, the magnitude of pressure gradient. The relative permeability k_{rj} of each phase is given by

$$k_{rj} = k_{rj}^0 \left(\frac{S_{j,a} - S_{jr}}{1 - S_{wc} - S_{or} - S_{gr}} \right)^{n_j}, \tag{5}$$

where k_{rj}^0 is the endpoint relative permeability, $S_{j,a}$ is the absolute saturation, S_{jr} is the residual saturation (S_{wc}, S_{or} or S_{gr}), and n_j is the Corey exponent. (See Appendix A for the parameter values used in this study).

Substituting Eq. (4) into Eq. (3) transforms f_j to:

$$f_j = \frac{k_{rj}/\mu_j}{k_{rw}/\mu_w + k_{ro}/\mu_o + k_{rg}^f/\mu_g}, \tag{6}$$

where (k_{rj}/μ_j) denotes the relative mobility of phase j. k_{rg}^f denotes the effective gas relative permeability k_{rg} altered by foam through a mobility reduction factor FM (see description of STARS model in Appendix A). For simplifications, we ignore the effects of gravity and of capillary-pressure gradients on f_j (note: capillary effects are very important to foam properties, which is accounted for in the mobility-reduction factor by foam, FM. The effect ignored here is flow driven by capillary-pressure gradients). FM is a function of S_w and S_o, so f_j is a function of only saturations (S_w, S_o).

To simplify Eqs. (1) and (2), we introduce dimensionless variables x_D and t_D:

$$x_D \equiv \frac{x}{L}, \tag{7}$$

$$t_D \equiv \frac{u \cdot t}{(1 - S_{wc} - S_{or} - S_{gr}) L \varphi}, \tag{8}$$

where L is the reservoir length and t_D is the number of movable pore volumes injected, denoted as PVI. Also, we use saturations S_j normalized for residual saturations:

$$S_j \equiv \frac{S_{j,a} - S_{jr}}{1 - S_{wc} - S_{or} - S_{gr}}. \tag{9}$$

Using Eqs. (7)–(9), the system of Eqs. (1) and (2) is simplified to

$$\frac{d\mathbf{S}}{dt_D} + \frac{d\mathbf{F}}{dx_D} = 0, \tag{10}$$

where $\boldsymbol{S}$ and $\boldsymbol{F}$ are vectors $\begin{pmatrix} S_w \\ S_o \end{pmatrix}$ and $\begin{pmatrix} f_w \\ f_o \end{pmatrix}$, respectively.

Fractional-flow theory solves for a displacement by solving for velocities of S_w, S_o and S_g along a displacement path from injection state (J) to initial state (I). Three-phase fractional-flow theory demonstrates that saturation velocities are equal to the derivative of f_i with respect to S_i, i.e. eigenvalues of the Jacobian matrix (Lake et al., 2014):

$$\eta(\mathbf{S}) \equiv \frac{dx_D}{dt_D} = \frac{\partial f_j}{\partial S_j}. \tag{11}$$

In this study, we employ the exact Riemann Problem solver in n-dimensions, RPn, which implements the WCM to compute saturation paths (Azevedo et al., 2010; Castañeda et al., 2016; Furtado, 1991; Liu, 1974; Tang et al., 2019c). The RPn solver is based on the fundamentals of systems of conservation laws, e.g. rarefaction and shock curves derived from Hugoniot loci, accounting for complex bifurcation structures that may arise. Its numerical implementation incorporates ordinary-differential-equation solvers and algebraic-curve reconstruction techniques. A more recent version for 2 × 2 systems, named ELI, is available at [https://eli.fluid.impa.br/], see Castañeda et al. (2022). The principle of the WCM has been elaborated in the literature (Castañeda, 2018; Castañeda et al., 2016, 2022; Tang et al., 2019c). In general, the WCM constructs a displacement path by solving for two families of wave curves: a forward slow-wave curve calculated starting from injection state J and a backward fast-wave curve calculated starting from initial state I. The two families of wave curves usually cross, resulting in an intermediate state IJ at the intersection. A shock wave to the initial state is solved via a continuation method of states that satisfy the Rankine-Hugoniot relation:

$$\boldsymbol{F}(\mathbf{S}) - \boldsymbol{F}(\mathbf{S_I}) = \sigma(\mathbf{S} - \mathbf{S_I}), \tag{12}$$

where $\boldsymbol{S_I}$ denotes the saturations at I, and σ is the dimensionless shock velocity from $\boldsymbol{S_I}$ to $\boldsymbol{S}$. This relation effectively captures the shocks between saturation states. The solutions by the WCM here are stable with time. A complete path comprises saturations from J to IJ, and then to I. Based on saturations along a path and their velocities, one can construct saturation distributions, $S_j(x_D, t_D)$. The saturation profiles we show below give a good agreement with numerical simulation results as verified in Lyu et al. (2021).

2.2. Representation of foam by the STARS model

In the STARS model, foam is represented via a mobility-reduction factor, FM in Eq. (A-2), which reduces k_{rg}. FM incorporates a series of functions F_1 to F_6, accounting for effects of various factors on foam. The key factors affecting foam behavior are water- and oil-related parameters. Thus, we consider two key functions: F_2 in Eq. (A-3) for the effect of S_w, and F_3 in Eq. (A-8) for the effect of S_o. Taken together, these two functions represent the two flow regimes of foam shown in Fig. 1. The arctangent function for F_2 is approximated using a 5-degree polynomial function in Eq. (A-7) that gives a good approximation of F_2 (see Appendix A). The approximated polynomial function greatly facilitates the calculation of fractional-flow derivatives. Other factors, e.g. surfactant concentration and shear-thinning behavior, which are also important to the effectiveness of foam mobility control, need further research in the future.

Fig. 2 shows a map of foam properties characterized by the values of $(1/FM)$ in ternary saturation space. The values of $(1/FM)$ split the ternary diagram into two regions: the foam region with $(1/FM) > 1$, i.e. the colored lower-left patch, and the no-foam region with $(1/FM) = 1$, i.e. the white portion. The foam region is bounded by water- and oil-saturation-related model parameters, e.g. the limiting water saturation $fmdry$ in Eq. (A-3) and the lower- and upper-limiting oil saturations, $floil$ and $fmoil$ in Eq. (A-8). Since no measured data are reported on $floil$ and $fmoil$, their values are chosen for illustration purpose.

Along the direction parallel to the gas-oil binary, for $S_w < (fmdry - \varepsilon)$ where $\varepsilon = 1/(2 \times epdry)$, foam is too dry to be maintained. For ($fmdry$ –

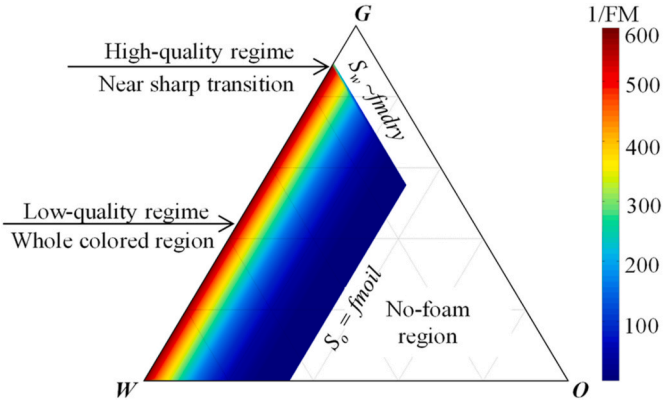

Fig. 2. Gas-mobility-reduction factor $(1/FM)$ plotted as a function of (S_w, S_o) in ternary saturation space. Model parameters are given in Appendix A. Three vertices, G, O, and W, represent 100 % normalized saturations (Eq. (9)) of gas, oil and water, respectively. Thus, in this and subsequent plots, $S_j = 0$ at the edges corresponds to residual saturations S_{gr}, S_{or} or S_{wc}.

$\varepsilon) \leq S_w \leq (fmdry + \varepsilon)$, $(1/FM)$ rises suddenly and abruptly, corresponding to the high-quality regime in Fig. 1. For $S_w \geq (fmdry + \varepsilon)$, strong foam is present, corresponding to the low-quality regime. The transition between the two regimes occurs near $S_w \approx fmdry + \varepsilon$, which is not visible here due to a very small value of ε, reflecting a sharp transition.

Along the direction parallel to the gas-water binary, for $S_o \leq floil$, F_3 in Eq. (A-8) equals unity, meaning that oil has no destabilizing effect on foam. For $floil < S_o < fmoil$, F_3 decreases with S_o, and so does $(1/FM)$, representing a non-linear destabilizing effect of oil on foam. For $S_o > fmoil$, $F_3 = 0$ and $(1/FM) = 1$, i.e. that oil completely destroys foam.

3. Results and discussion

Table 1 summarizes the representative cases we solve for immiscible foam flooding with oil. These cases fall into two scenarios, with initial oil saturation (S_{oi}) stable or unstable for foam, respectively. In each scenario, foam is injected either in the low- or high-quality regime. The model parameters used here for foam without oil are from the model fit of Cui et al. (2016) to CO_2 foam data at high pressure and high temperature.

3.1. Initial state stable for foam ($S_{oi} < fmoil$)

3.1.1. Foam injection in the low-quality regime

Here we discuss low-quality foam injection, displacing an initial state I that allows a weak or strong foam, respectively, where S_{oi} at I does not kill foam. Fig. 3 shows the fractional-flow solutions for I allowing a weak foam ($S_{oi} = 0.3$ and $fmoil = 0.35$) and Fig. 4 for I allowing a strong foam ($S_{oi} = 0.05$ and $fmoil = 0.35$), both with foam injection at $f_g = 0.5$. The fractional-flow solutions for each case give a composition path and saturation velocities and total relative mobility along the path.

(1) Effectiveness of foam mobility control with oil allowing a weak or strong foam. Regardless of S_{oi} allowing a weak or strong foam, the composition paths in Figs. 3 and 4 both reside within the foam region, i.e. $S_w > fmdry$ and $S_o < fmoil$ everywhere along the paths. This means that with I stable for foam, the whole displacement maintains a stable foam, suggesting effective mobility control in the entire displacements. This result is also supported by the total relative mobility trend along the paths (boxed numbers marked in Fig. 3b and 4b):

$$\lambda_{rt} = k_{rw}/\mu_w + k_{ro}/\mu_o + k^f_{rg}/\mu_g. \tag{13}$$

The values of λ_{rt} decrease from I back to J, confirming the effectiveness of foam mobility with oil. This further implies that gas fingering would be mitigated in 2D or 3D porous media in similar cases.

(2) Oil-bank creation by foam. The forward slow-wave curve starting from J (blue) and backward fast-wave curve initiating from I (red) intersect, resulting in the intermediate state IJ (Liu, 1974; Castañeda et al., 2016). This state corresponds to S_o in the oil bank. Since the whole path resides within the foam region, S_o in the oil bank nowhere exceeds $fmoil$, the upper bound for stable foam.

(3) Foam and oil-bank propagation. The propagation of an oil bank is driven by foam. Here we identify key factors that control foam propagation: maximum S_o for stable foam, foam quality, and foam strength at J and at I (when oil is present). The mechanism of each factor is as follows:

- Maximum S_o for stable foam. Without oil, foam propagates as far as where surfactant and gas are both present. With oil, foam propagation is restricted by an additional factor – foam stability with oil, since for $S_o > fmoil$, foam is killed completely by oil.
- Foam quality. For a stable foam in terms of both S_w and S_o, foam propagation depends on injected foam quality f_g and a material balance on gas. S_g in the foam-swept zone remains high and does not change much for a wide range of f_g. Therefore, increasing injected f_g, when still maintaining adequate foam strength, accelerates foam propagation, when surfactant is not limiting.
  Our model assumes that surfactant propagation is not a limitation. In a process without surfactant initially in the reservoir, increasing injected f_g, by reducing surfactant and water injection rate, can slow foam propagation by slowing surfactant propagation into the reservoir (Lake et al., 2014).
- Foam strength at J. The impact of foam strength on foam propagation is associated with its correlation with f_g. For foam injection in the low-quality regime, stronger foam corresponds to greater f_g, thus giving faster foam propagation. For foam injection in the high-quality regime, stronger foam corresponds to lower f_g, meaning slower foam propagation. For foam injection at the same f_g, stronger foam (e.g. due to more effective surfactant) means greater S_g in the foam zone and thus slower foam propagation, as seen from material balance on gas.
- Foam strength at I. With oil, efficient foam propagation requires that foam be stable and have sufficient strength at the displacement front to avoid significant gas escaping ahead of the foam. Thus, the stronger the foam is at I, the faster the foam propagation would be.

Comparing the propagation of foam banks between Fig. 3b and 4b confirms the effect of foam strength at I on foam propagation. The mobility reduction factor $(1/FM) = 13$ at high S_{oi} in Fig. 3 and $(1/FM) = 433$ at low S_{oi} in Fig. 4. The foam bank with stronger foam at I in Fig. 4b propagates at a dimensionless velocity six times faster than the weaker foam at I in Fig. 3b. The faster foam-bank propagation is a result of

Table 1
Summary of representative foam displacement cases with various combinations of J and I.

Cases		Injection condition $J = (S_w, S_g), f_g$	Initial condition $I = (S_w, S_o)$	Remarks on foam strength at J & I, respectively
Initial state, I stable for foam ($S_{oi} < fmoil$)	1a	$J = (0.108158, 0.891842), f_g = 0.5$	$I = (0.7, 0.3)$	$(\text{Strong foam})_L$ & $(\text{Weak foam})_I$
	1b	$J = (0.108158, 0.891842), f_g = 0.5$	$I = (0.95, 0.05)$	$(\text{Strong foam})_L$ & $(\text{Strong foam})_I$
	1c	$J = (0.105214, 0.894786), f_g = 0.9$	$I = (0.7, 0.3)$	$(\text{Weak foam})_H$ & $(\text{Weak foam})_I$
	1d	$J = (0.105214, 0.894786), f_g = 0.9$	$I = (0.95, 0.05)$	$(\text{Weak foam})_H$ & $(\text{Strong foam})_I$
	1e	$J = (0.165, 0.835), f_g = 0.3$	I =(0.7, 0.3)	$(\text{Weak foam})_L$ & $(\text{Weak foam})_I$
	1f	$J = (0.108158, 0.891842), f_g = 0.5$	$I = (0.7, 0.3)$	$(\text{Strong foam})_L$ & $(\text{Weak foam})_I$ $floil = 0.2$, $fmoil = 0.5$
Initial state, I unstable for foam ($S_{oi} > fmoil$)	2a	$J = (0.108158, 0.891842), f_g = 0.5$	$I = (0.2, 0.8)$	$(\text{Strong foam})_L$ & $(\text{No foam})_I$
	2b	$J = (0.105214, 0.894786), f_g = 0.9$	$I = (0.2, 0.8)$	$(\text{Weak foam})_H$ & $(\text{No foam})_I$
	2c	$J = (0.108158, 0.891842), f_g = 0.5$	$I = (0.2, 0.8)$	$(\text{Strong foam})_L$ & $(\text{No foam})_I$ $floil = 0.2$, $fmoil = 0.5$

Note that all saturations and $fmoil$ and $floil$ shown here are normalized for residual saturations using Eq. (9). Foam model parameters are given in Appendix A, except where noted in the final column. Subscripts L and H in remarks denote foam injection in the low- and high-quality regime, respectively.

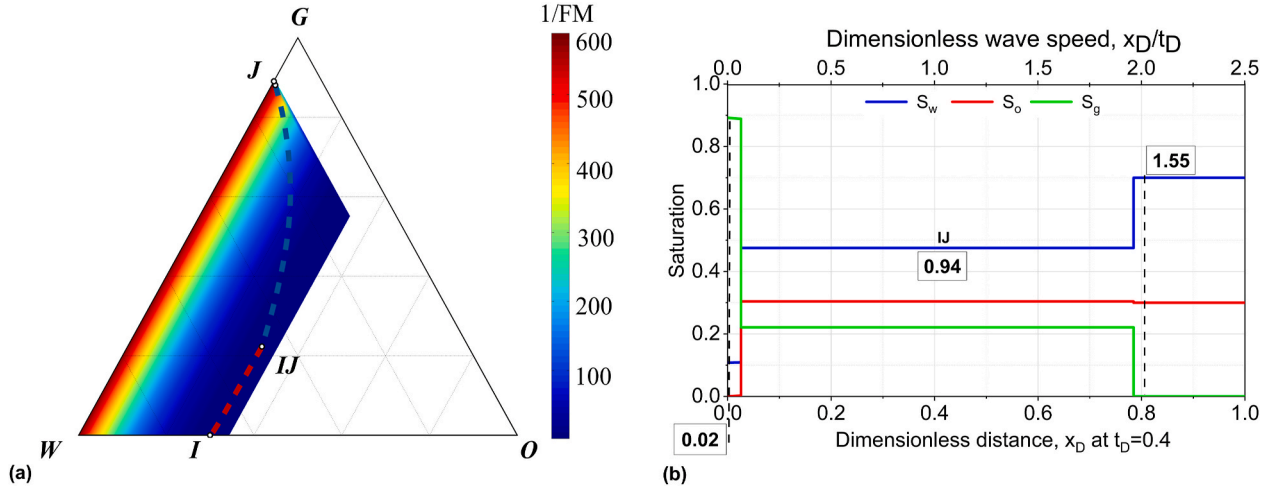

Fig. 3. (a) Composition path for Case 1a: foam injected at $f_g = 0.5$ displacing I allowing a weak foam (S_{oi} less than but close to *fmoil*); **(b)** Saturation velocities (on the top axis) and positions at $t_D = 0.4$ PVI (on the bottom axis) along the path. Solid and dashed lines in Fig. 3a denote spreading and shock waves, respectively. Boxed numbers in Fig. 3b mark λ_{rt} (Eq. (13)) in units (1/cp) at the position indicated by the vertical dashed lines. The same definitions for the solid and dashed lines and boxed numbers apply in the subsequent plots.

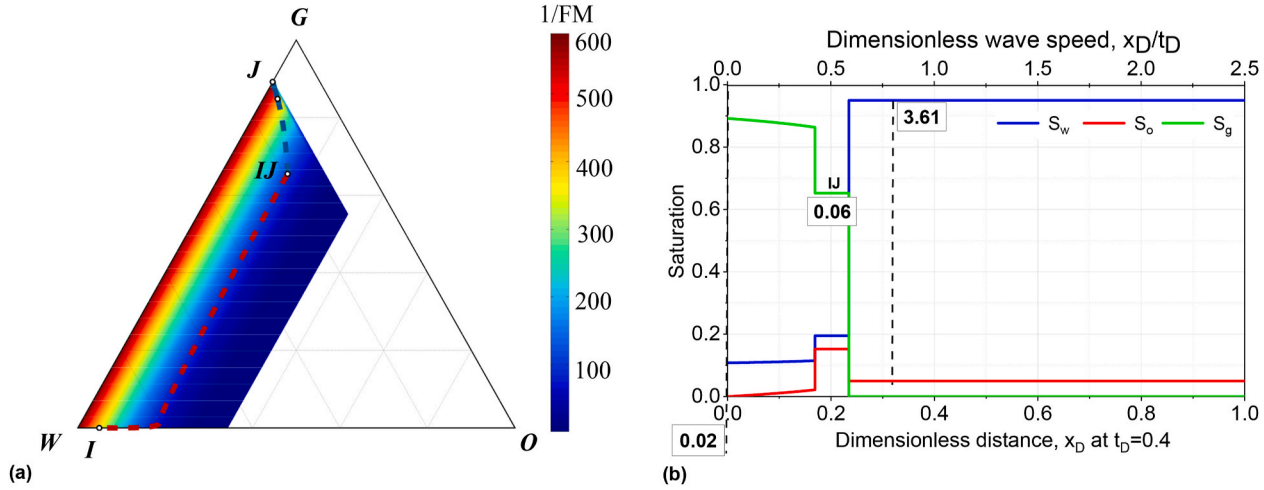

Fig. 4. (a) Composition path for Case 1b: foam injected at $f_g = 0.5$ displacing I allowing a strong foam (S_{oi} far less than *fmoil*); **(b)** Saturation velocities (on the top axis) and positions at $t_D = 0.4$ PVI (on the bottom axis) along the path.

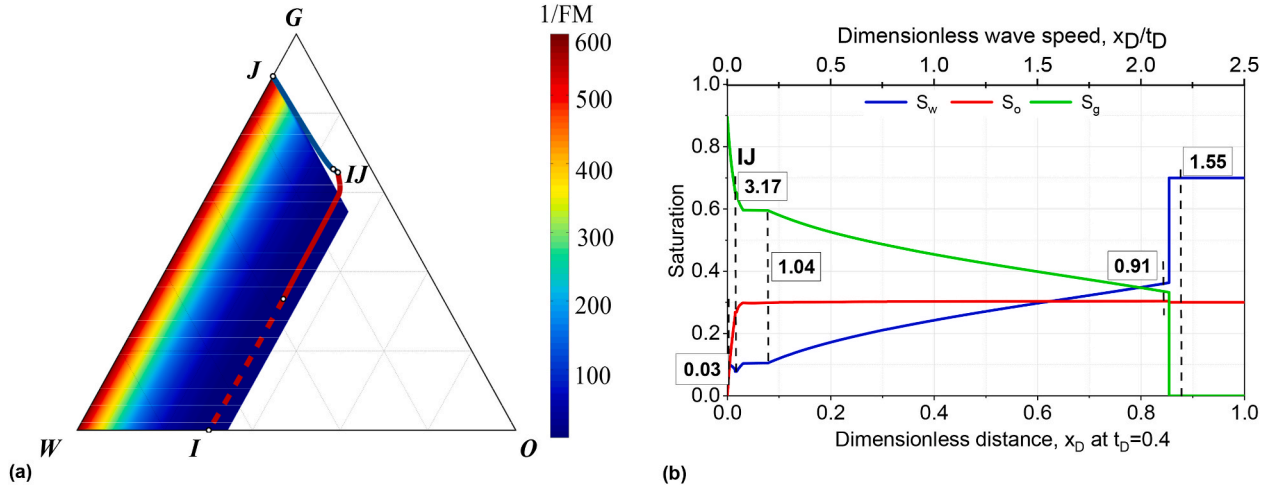

Fig. 5. (a) Composition path for Case 1c: foam injected at $f_g = 0.9$ displacing I allowing a weak foam (i.e. lower value of ($1/FM$) due to S_{oi} less than but close to *fmoil*); **(b)** Saturation velocities (on the top axis) and positions at $t_D = 0.4$ PVI (on the bottom axis) along the path.

stronger foam that reduces gas escaping ahead of the foam bank, as seen from the slower gas front in Fig. 4b compared to Fig. 3b. In addition, with $S_{oi} \ll fmoil$ in the case of Fig. 4, the stronger foam at I helps creation of a significant oil bank, with S_o in the oil bank constrained below *fmoil*.

3.1.2. Foam injection in the high-quality regime

Figs. 5 and 6 present the fractional-flow solutions for high-quality foam injection ($f_g = 0.9$) displacing S_{oi} at I that allows a weak or strong foam, respectively. $f_g = 0.9$ chosen here is within the range of foam qualities injected in the field, considering chemical cost and foam strength desired. The foam injected at J has $(1/FM) = 241$ in both cases, and initial state I allows a foam with $(1/FM) = 13$ and 433 in the cases of Figs. 5 and 6, respectively.

In contrast to low-quality foam, with high-quality foam, a portion of the path around the intermediate state IJ goes into the no-foam region, in both cases of Figs. 5 and 6, although I in the case of Fig. 6 allows a strong foam. Without foam, gas mobility is high, leading to unstable displacement front and early gas breakthrough. The foam collapse here arises from a dry-out effect due to low S_w (i.e. S_w lower than $fmdry = 0.1053$), not the effect of high S_o. As a result, λ_{rt} does not decrease monotonically from I back to J as with low-quality foam injection, but with λ_{rt} near IJ much higher than λ_{rt} at J and I (Fig. 5b and 6b). This implies less-effective mobility control with foam injection in the high-quality regime than in the low-quality regime, e.g. $\lambda_{rt} = 4.20$ at state IJ, also greater than 0.03 at J and 3.61 at I in Fig. 6b. Such trend in λ_{rt} along a displacement path indicates that gas fingering would be an issue in the 3D media.

The contrast in the effectiveness of foam with oil between high- and low-quality foam injection (Figs. 3 and 4 vs. Figs. 5 and 6) suggests an optimal injection strategy: inject foam in the low-quality regime near the transition foam quality f_g*. With foam injection in the low-quality regime, a stable foam is sustained in the entire displacement, regardless of S_{oi} at I that allows a strong or weak foam. This further suggests that, in addition to foam strength, the regime in which foam is injected is another crucial factor to consider in the design of foam EOR for CO_2 sequestration. This argument is verified by Case 1e as shown in Fig. 7, where foam is injected in the low-quality regime but with a weaker strength than in Figs. 5 and 6. The low-quality foam injection, although with a weaker strength, still yields a path that entirely resides inside the foam region. This confirms the importance of the regime in which foam is injected. Thus, field applications should select injection parameters that give a foam in the low-quality regime, in addition to maximizing foam strength.

The rule we find for the optimal injection strategy is based on the foam-model parameters fitted for a CO_2 foam in carbonate rocks at high temperature (Cui et al., 2016). The universality of this rule needs to be verified for a wide range of model parameters, e.g. *fmdry*, *fmmob*, *floil*, *fmoil* and *epoil*.

3.2. Initial state unstable for foam ($S_{oi} > fmoil$)

Here we examine the feasibility of foam applications when initial oil saturation S_{oi} is too high to allow a stable foam for the given surfactant formulation. The behavior and mechanisms are analyzed for foam injection in the high- and low-quality regime, respectively.

3.2.1. Foam injection in the low-quality regime

Fig. 8 shows the displacement behavior with foam injected in the low-quality regime at $f_g = 0.5$ with $(1/FM) = 589$. Fig. 8a shows the composition path and Fig. 8b shows the saturation profiles. The wave structure of this case consists of a spreading wave and shock from J within the foam region and then a spreading wave, shock to IJ and spreading wave to I outside the foam region. The saturation profiles reveal that the mechanisms of foam displacing S_{oi} unstable for foam combine two processes: waterflooding ahead followed by slowly advancing foam flood. The waterflooding banked up by foam reduces S_o below *fmoil* ahead, a key that allows the propagation of foam.

The values of λ_{rt} indicate that the water-oil mobility ratio is unfavorable and may result in fingering. Thus, just by waterflooding, it may be difficult to reduce S_o low enough to allow for subsequent strong foam displacement and fast foam propagation. This indicates a role polymer might play in helping foam with oil: the addition of polymer could reduce the fingering and speed the reduction in oil saturation ahead of the foam. In addition, sufficient foam strength in contact with high S_o is also necessary to prevent gas escaping ahead of the foam bank. In Fig. 8b, 88% of the injected gas escapes ahead of the foam bank.

3.2.2. Foam injection in the high-quality regime

Fig. 9 shows the displacement solutions with foam injected in the high-quality regime at $f_g = 0.9$ with $(1/FM) = 241$. The composition path crosses the foam boundary at $S_w \sim fmdry$, instead of the boundary at $S_o = fmoil$ as in Fig. 8a. This indicates that foam collapse here is a result of the drying-out effect ($S_w < fmdry$), not the effect of high S_o. When foam collapses starting a short distance from the injection well, it fails to bank up water to displace oil ahead. As a result, gas escapes ahead of the foam, restricting foam propagation. The values of λ_{rt} in Fig. 9b also suggest significant gas fingering in this case, and this issue would get worse in 3D systems due to formation heterogeneity and gravity override.

Figs. 8 and 9 consistently show that foam injection in the low-quality

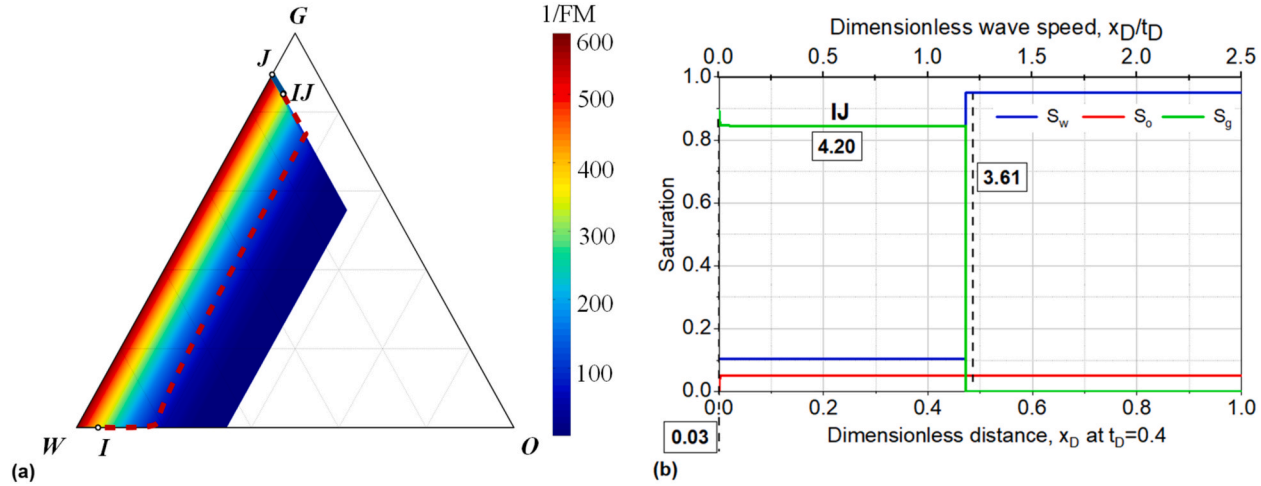

Fig. 6. (a) Composition path for Case 1d: foam injected at $f_g = 0.9$ displacing I allowing a strong foam (S_{oi} far less than *fmoil*); **(b)** Saturation velocities (on the top axis) and positions at $t_D = 0.4$ PVI (on the bottom axis) along the path.

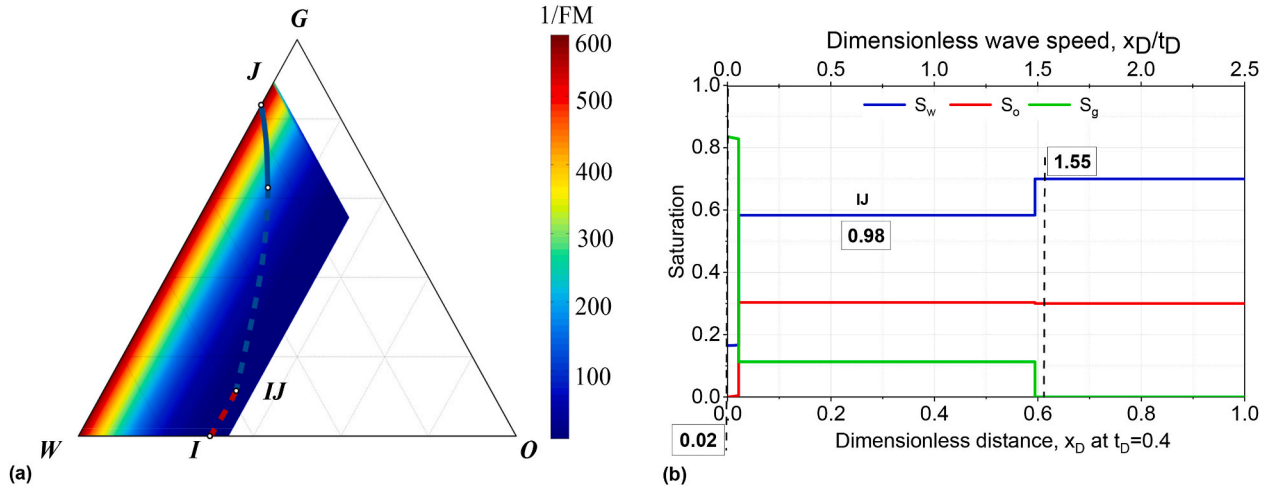

Fig. 7. (a) Composition path for Case 1e: foam with weak strength injected at $f_g = 0.3$ displacing I that allows a weak foam; **(b)** Saturation velocities (on the top axis) and positions at $t_D = 0.4$ PVI (on the bottom axis) along the path.

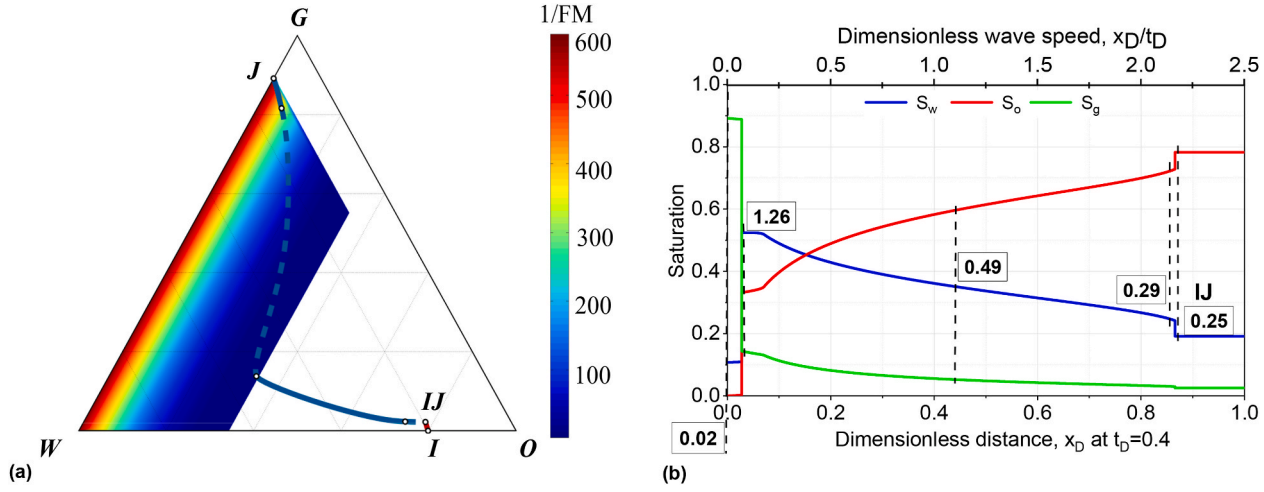

Fig. 8. (a) Composition path for Case 2a: foam injected at $f_g = 0.5$ displacing I unstable for foam ($S_{oi} > fmoil$); **(b)** Saturation velocities (on the top axis) and positions at $t_D = 0.4$ PVI (on the bottom axis) along the path.

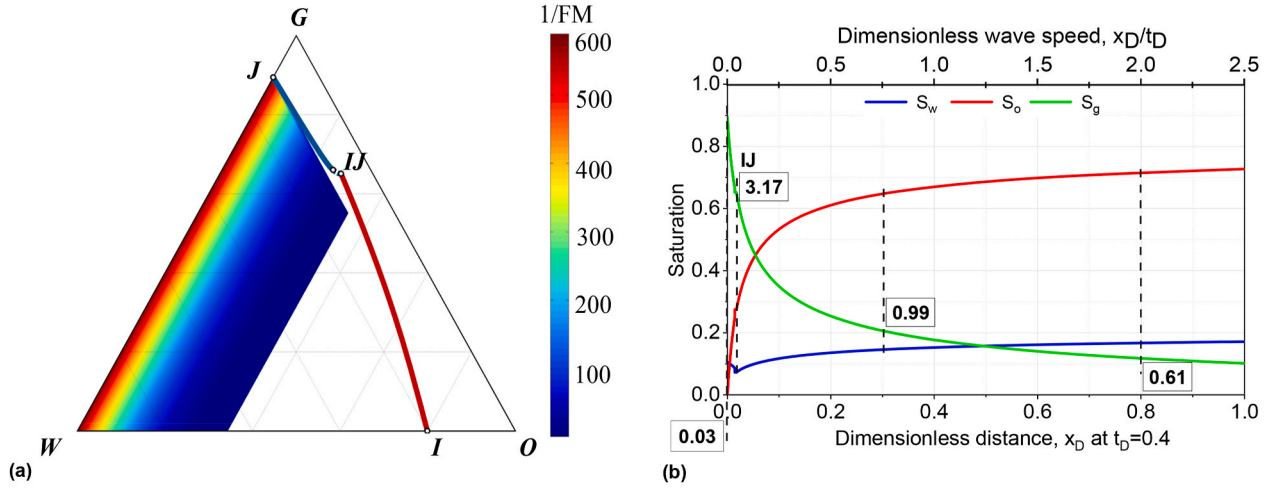

Fig. 9. (a) Composition path for Case 2b: foam injected at $f_g = 0.9$ displacing I unstable for foam ($S_{oi} > fmoil$); **(b)** Saturation velocities (on the top axis) and positions at $t_D = 0.4$ PVI (on the bottom axis) along the path.

regime is more effective than in the high-quality regime. This confirms again that both foam strength and the regime in which foam is injected are crucial factors to consider in the field design of foam injection processes. To allow for foam injection at high f_g while still remaining in the low-quality regime, one solution would be a surfactant formulation that gives a lower value of *fmdry* (i.e. foam stable at drier conditions).

3.3. Effect of improved foam tolerance to oil

In a widely used foam model, STARS, the oil effect is represented by parameters *floil* (lower bound in S_o, above which oil starts destabilizing foam) and *fmoil* (upper bound in S_o, above which foam is killed by oil). Here we show the effects of improved foam tolerance to oil under the scenarios of initial oil saturation S_{oi} stable or unstable for foam, respectively. The effects are analyzed through its impact on mobility control, oil-bank creation and foam propagation.

3.3.1. Effect of improved foam tolerance to oil with $S_{oi} <$ *fmoil*

Fig. 10 shows the results for foam displacing *I* stable for foam, where *floil* is raised to 0.2 and *fmoil* is raised to 0.5, for comparison to Fig. 3. The changes in foam tolerance to oil do not change the basic wave structure along the path (see Fig. 3a and 10a).

Improving foam tolerance to oil has multiple benefits: (1) expanding the range of S_o where oil has no impact on foam when *floil* is increased, as indicated by the dark-red region in Fig. 10a, and allowing a wider range of S_o for stable foam when *fmoil* is increased (compare Fig. 3a and 10a); (2) promoting oil-bank creation when *fmoil* is moved further above S_{oi}; (3) accelerating foam propagation, since stronger foam in contact with oil reduces gas escaping and retains gas in the foam zone. The propagation of this foam is still slow, i.e. at a dimensionless velocity of 0.31 in Fig. 10b. Allowing for stronger foam at S_{oi} and thus faster foam propagation in the presence of oil requires the foam region to go deeper into the phase diagram.

The better foam tolerance to oil enhances ($1/FM$) at *I* from 13 in Figs. 3 to 262 in Fig. 10. As a result, foam creates an oil bank with a greater S_o and propagates faster, in comparison to Fig. 3. Thus, sufficient foam tolerance to oil (i.e. high value of ($1/FM$)) is crucial to the oil-displacement and foam-propagation efficiency in the field. Furthermore, all the cases (Figs. 3, 4 and 10) under the scenario of foam displacing *I* stable for foam show that S_o in the oil bank displaced by foam lies within the range: $S_{oi} < S_o <$ *fmoil*. More significantly, this constraint suggests a criterion for creating a substantial oil bank by foam: *fmoil* must be further above initial oil saturation S_{oi}. Only when *fmoil* is further above S_{oi} can it allow substantial accumulation of oil in the oil bank. This criterion is a general rule and its generality is justified in Section 3.4 below.

3.3.2. Effect of improved foam tolerance to oil with $S_{oi} >$ *fmoil*

Fig. 11 shows the results for foam displacing *I* unstable for foam, where *floil* is raised to 0.2 and *fmoil* is raised to 0.5, for comparison to the case in Fig. 8. The changes in *floil* and *fmoil* again do not change the basic wave structure along the path from *J* to *I* (cf. Fig. 8a and 11a).

Similar to the scenario with $S_{oi} <$ *fmoil* above, raising *floil* expands the dark-red region where oil has no impact on foam, and raising *fmoil* expands the region for stable foam (compare Fig. 11a with Fig. 8a). The enhanced foam tolerance to oil improves mobility control, e.g. $\lambda_{rt} = 0.57$ in Fig. 11b compared to 1.26 in Fig. 8b ahead of the foam bank. Stronger foam at *I* accelerates foam propagation. However, S_o ahead of the foam bank still stays close to *fmoil*, yielding a weak foam ahead, leading to gas escape and slow foam propagation. In Fig. 11b, 66% of injected gas escapes ahead of the foam bank. Polymer injection ahead of foam may accelerate reduction in S_o ahead, accelerating foam propagation and reducing gas escape.

In addition, cases (Figs. 8 and 11) in this scenario have a trend with increasing λ_{rt} from *I* back to the front of the foam bank. This λ_{rt} trend implies water/gas fingering in the field and further slows foam propagation. Thus, it may be more favorable to conduct water or polymer flood first to reduce S_o ahead below *fmoil*, followed by foam flood, which converts to the scenario with S_{oi} stable for foam.

3.4. Generality of the criterion $S_o <$ *fmoil* in foam-created oil banks

Fractional-flow theory states that velocities of saturations (given in Eqs. (11) and (12)) along a displacement path from *J* to *I* must be monotonically increasing (Lake et al., 2014). Suppose foam creates an oil bank with $S_o >$ *fmoil*, e.g. in the case modelled in Fig. 10. Immediately behind the oil bank, foam is present and reduces gas mobility substantially, leading to water fractional flow $f_w \gg 0$ behind the oil bank. Within the oil bank, if $S_o >$ *fmoil*, foam is killed completely, leading to high gas mobility and S_o and thus reduced f_w. However, S_w in the foam bank is lower than S_w in the oil bank. The decrease in f_w and increase in S_w across the shock displacing the oil bank results in a negative shock velocity (Eq. (12)). This negative velocity is physically impossible; it violates the velocity compatibility required for a forward displacement (Tang et al., 2019c).

For instance, in Fig. 10b, for the state with foam immediately behind the oil bank, $(S_w, f_w) = (0.107740, 0.52)$ and for the state in the oil bank $(S_w, f_w) = (0.309594, 0.73)$, resulting in $(\Delta f_w/\Delta S_w) = 1.04$. Suppose in

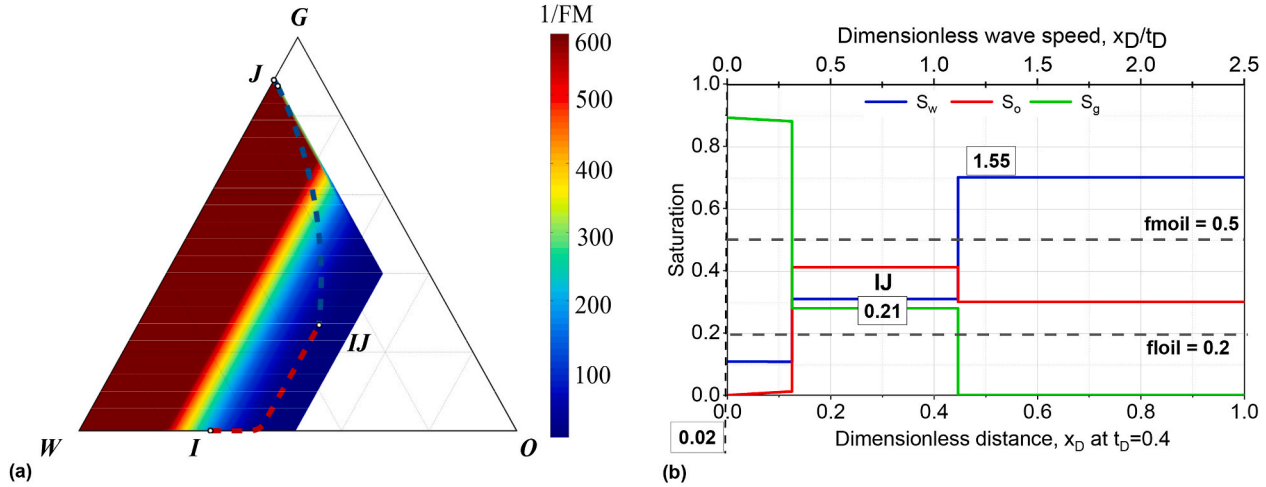

Fig. 10. (a) Composition path for Case 1f with $S_{oi} <$ *fmoil*: *floil* increased to 0.2 and *fmoil* increased to 0.5, for comparison to Case 1a in Fig. 3; **(b)** Saturation velocities (on the top axis) and positions at $t_D = 0.4$ PVI (on the bottom axis) along the path, where the horizontal dashed lines mark the values of *floil* and *fmoil*.

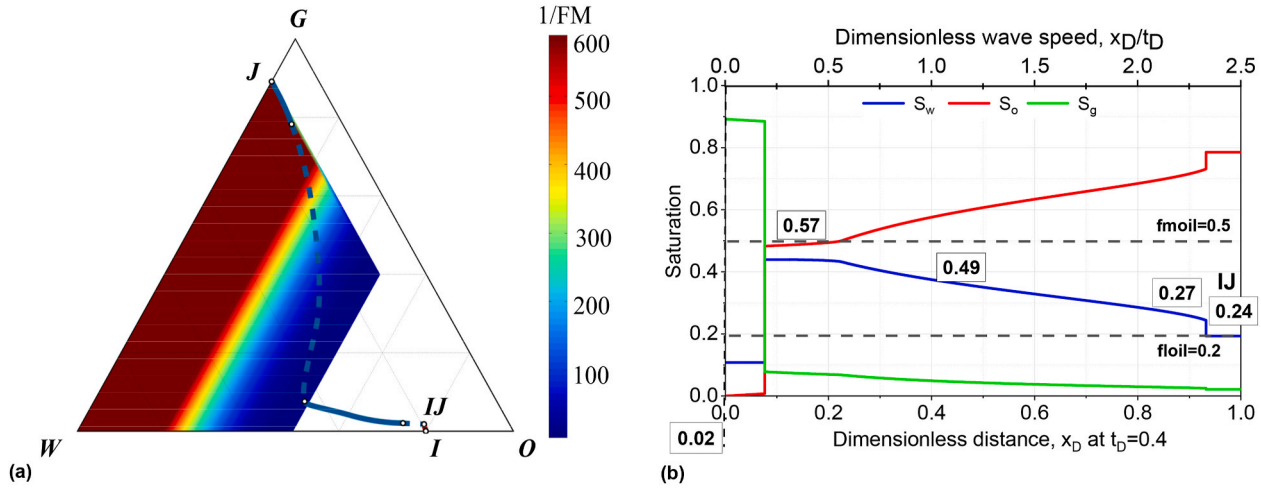

Fig. 11. (a) Composition path for Case 2c with $S_{oi} > fmoil$: *floil* increased to 0.2 and *fmoil* increased to 0.5, for comparison to Case 2a in Fig. 8; (b) Saturation velocities (on the top axis) and positions at $t_D = 0.4$ PVI (on the bottom axis) along the path, where the horizontal dashed lines mark the values of *floil* and *fmoil*.

the oil bank, $S_o = 0.51$ (i.e. greater than $fmoil = 0.5$) and S_g is the same as the first case; the oil bank then has $(S_w, f_w) = (0.2111359, 0.04)$ and the foam immediately behind the oil bank has $(S_w, f_w) = (0.107740, 0.52)$. The shock velocity across the leading edge of the foam bank is $(\Delta f_w/\Delta S_w) = -4.66 < 0$.

Therefore, it is a general rule that S_o in an oil bank displaced by foam can never exceed *fmoil*. It demonstrates the generality of the criterion for creation of a substantial oil bank by foam as well: *fmoil* must be much greater than initial oil saturation S_{oi} to allow for significant banking up of oil.

Numerical simulations sometimes show $S_o > fmoil$ in the oil bank created by foam. This violation of fractional-flow theory may reflect a numerical artifact in the standard finite-difference simulation of foam displacement with oil (Tang et al., 2022). Here we simply illustrate the artifact from the results published in the literature, as shown in Fig. 12.

As illustrated in Fig. 13, suppose the interface between grid blocks (i-1) and i corresponds to the foam-displacement front. When $S_o > fmoil$ in grid block i, physically it prevents foam from propagation into grid block i and thus oil is drained out of grid block i into (i+1) very slowly either by water or gas. Nevertheless, numerical simulation still gives a fast foam propagation. This may arise from the calculation of fluxes that flow

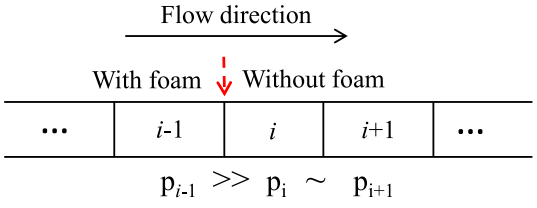

Fig. 13. Schematic of calculation of pressure in each grid block using pressures in neighboring grid blocks in finite-difference simulation.

into or out of grid block i. The calculation of fluxes may be problematic either due to the calculation of phase mobilities using upstream weighting or the calculation of pressure gradient in the displacement grid block based on pressures in the neighboring upstream and downstream grid blocks.

Further research is needed to identify specific causes of this possible artifact and other possible issues with calculation of pressure gradient in foam simulations (Yu and Rossen, 2022; Tang et al., 2025).

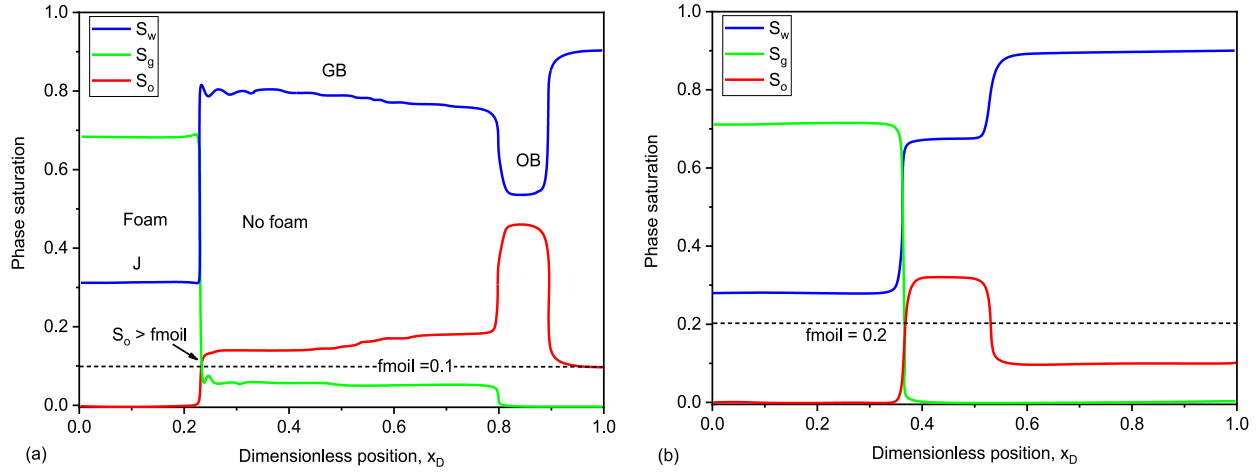

Fig. 12. 1D numerical simulations of foam displacement with immiscible oil using STARS foam model: **(a)** adapted from Liu et al. (2011) for partially miscible displacement (CO_2 displacing C_{14}) after 0.5 PV foam injection, and **(b)** adapted from Dharma (2013) for immiscible displacement (N_2 displacing C_{12}) after 0.3 PV foam injection.

4. Conclusions

Three-phase fractional-flow theory demonstrates that oil saturation (S_o) in the oil bank, if created by foam, never exceeds the upper bound for stable foam, *fmoil*. This means that S_o in the oil bank must lie within the range S_{oi} (initial oil saturation) $< S_o <$ *fmoil*.

This constraint means that for foam to create a significant oil bank, *fmoil* needs to be far above S_{oi}.

We identify key factors that control foam and oil-bank propagation: maximum oil saturation for stable foam (*fmoil*), foam quality (f_g), and foam strength at injection and initial states. The mechanisms of these factors are revealed via a material balance on gas: any factor that increases gas volume injected while maintaining adequate foam strength, or that reduces gas saturation in the foam region, accelerates foam and oil-bank propagation and vice versa.

The fractional-flow solutions imply an optimal injection strategy: inject foam in the low-quality regime near the transition foam quality. Unlike high-quality foam, low-quality foam injection sustains a stable foam in an entire displacement. Thus, not only foam strength but also the regime in which foam is injected is crucial to foam mobility control with oil. The generality of this rule needs to be further verified.

Numerical simulations sometimes show $S_o >$ *fmoil* in the oil bank. This reflects a possible numerical artifact, which may result in overstating the effectiveness of foam EOR for carbon sequestration. Further research is needed to investigate the causes for this possible numerical artifact.

The three-phase fractional-flow solutions, free of numerical artifacts, can be used as benchmarks to calibrate numerical simulators or machine-learning models for foam EOR for carbon-sequestration processes.

CRediT authorship contribution statement

Jinyu Tang: Writing – review & editing, Writing – original draft, Visualization, Validation, Supervision, Resources, Project administration, Methodology, Investigation, Funding acquisition, Formal analysis, Data curation, Conceptualization. **Pablo Castañeda:** Writing – review & editing, Visualization, Validation, Software, Resources, Methodology, Investigation, Funding acquisition, Data curation. **Dan Marchesin:** Writing – review & editing, Supervision, Software, Resources, Methodology. **William R. Rossen:** Writing – review & editing, Supervision, Methodology, Investigation, Formal analysis, Conceptualization.

Declaration of competing interest

The authors declare that they have no known competing financial interests or personal relationships that could have appeared to influence the work reported in this paper.

Acknowledgement

This project was funded by the UAEU Research Grant (12N099), UPAR (UAEU Program on Advanced Research) Grant (12N235) and partly by the National Council of Science and Technology (CONACYT) (A1-S-26012). P. Castañeda also thanks the Asociación Mexicana de Cultura A.C. for the partial financial support.

Appendix A. Implicit-Texture Foam Model – STARS

In the STARS model (Computer Modeling Group, 2015), foam modifies gas relative permeability k_{rg} through a mobility-reduction factor *FM:*

$$k_{rg}^{f} = k_{rg} \cdot FM, \tag{A-1}$$

where superscript *f* denotes the presence of foam. *FM* is given by

$$FM = \frac{1}{1 + fmmob \cdot F_1 \cdot F_2 \cdot F_3 \cdot F_4 \cdot F_5 \cdot F_6}, \tag{A-2}$$

where *fmmob* is the reference gas-mobility-reduction factor, denoting the maximum attainable gas-mobility reduction, and the F_i functions account for effects of various physical factors on foam properties. In this study, we consider two key functions, F_2 for the effect of S_w, and F_3 for the effect of S_o; thus *FM* is a function of only (S_w, S_o). These are the key to the two foam flow regimes in Fig. 1.

The water-saturation-dependent function F_2 is defined as follows:

$$F_2 = 0.5 + \frac{\arctan[epdry(S_w - fmdry)]}{\pi}, \tag{A-3}$$

where *fmdry* is the limiting water saturation below which foam collapses; the abruptness of foam collapse is controlled by an adjustable parameter, *epdry*. The model parameter values used here, fit to the experimental data (Cui et al., 2016), give a sharp transition between the two flow regimes and a large value of *epdry* gives an abrupt foam collapse at S_w around *fmdry*.

To simplify the calculation of derivatives of fractional flows in Eq. (11), F_2 in Eq. (A-3) is approximated here by a fifth-order polynomial function $p(x)$:

$$F_2 \cong p(x) = a + bx + cx^2 + dx^3 + ex^4 + fx^5, \tag{A-4}$$

where *a, b, c, d, e* and *f* are coefficients. Variable x is a function of S_w:

$$x = 2 \times epdry(S_w - fmdry), \tag{A-5}$$

where *epdry* and *fmdry* here have the same definitions as in Eq. (A-3).

The following six conditions are used to solve for the six coefficients in Eq. (A-4):

$$\begin{cases} p(-1)=0; & p(1)=1; \\ p'(-1)=0; & p'(1)=0; \\ p''(-1)=0; & p''(-1)=0. \end{cases} \tag{A-6}$$

Eq. (A-3) is then replaced by the following polynomial function:

$$F_2 \cong p(x) = \begin{cases} 0 & x<-1 \\ \dfrac{1+1.875x-1.25x^3+0.375x^5}{2} & -1\le x\le 1 \\ 1 & x>1 \end{cases}. \tag{A-7}$$

As shown in Fig. A-1, the polynomial approximation $p(x)$ matches the arctangent function F_2 closely. One major difference is that $p(x)=0$ for $S_w < \{fmdry - [1/(2\times epdry)]\}$ (i.e. $x<-1$) in Eq. (A-7), giving complete foam collapse. F_2 in Eq. (A-3) is close to but greater than 0 for any value of S_w when $S_w < fmdry$, meaning that foam becomes weaker but does not collapse completely for any S_w.

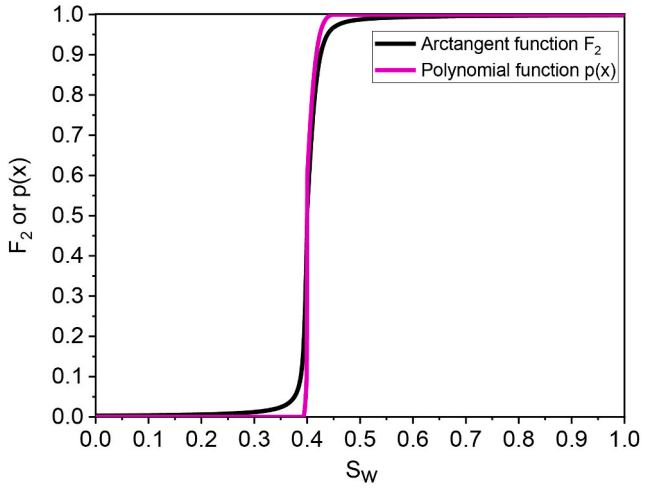

Fig. A-1. Comparison between the arctangent function F_2 in Eq. (A-3) and polynomial approximation $p(x)$ in Eq. (A-7). Model parameters are given in Table A-1 below.

The oil-saturation-dependent function F_3 is given by

$$F_3 = \begin{cases} 1 & S_{or}\le S_o\le foil \\ \left(\dfrac{fmoil-S_o}{fmoil-floil}\right)^{epoil} & floil<S_o<fmoil \\ 0 & fmoil\le S_o\le 1-S_{wc}-S_{gr} \end{cases}, \tag{A-8}$$

where *fmoil* is the upper-limiting oil saturation, above which foam is killed completely by oil, *floil* is the lower-limiting oil saturation below which oil has no impact on foam, and *epoil* is the oil exponent.

Table A-1 gives the values used here for parameters in a Corey-type relative-permeability model and STARS foam model, which were fit to the data by Cui et al. (2016) for CO_2 foam at high temperature in carbonate rocks. The foam-model parameters have a value of *fmmob* much less than some foams observed under conditions conducive to strong foam (Kim et al., 2005; Cheng et al., 2000; Boeije and Rossen, 2015). We choose a weaker foam here to account for, e.g., adverse wettability or high temperature in the field. These parameters are used in all the cases examined unless noted otherwise.

Table A-1
Parameter values used in the Corey-type relative-permeability and STARS foam models.

Corey-type relative-permeability model parameters and fluid properties						Foam model parameters		
k^o_{rw}	k^o_{ro}	k^o_{rg}	n_w	n_o	n_g	*fmmob*	*fmdry*	*epdry*
1	1	0.1768	2.8	2	1.1	588	0.39	1000
S_{wc}	S_{or}	S_{gr}	μ_w, cp	μ_o, cp	μ_g, cp	*fmoil*	*floil*	*epoil*
0.33	0.1	0	0.24	5	0.0351	0.3	0.1	3

Note that saturations and saturation-related parameters shown here are not normalized, while in Figs. 3–11, they are all normalized for residual saturations using Eq. (9).

Data availability

No data was used for the research described in the article.

References

Abbaszadeh, M., Varavei, A., Garza, F.R., Pino, A.E., Salinas, J.L., Puerto, M.C., Hirasaki, G.J., Miller, C.A., 2018. Methodology for the development of

laboratory–based comprehensive foam model for use in the reservoir simulation of enhanced oil recovery. SPE Reservoir Eval. Eng. 21 (2), 344–363.
Alvarez, J.M., Rivas, H.J., Rossen, W.R., 2001. Unified model for steady-state foam behavior at high and low foam qualities. SPE J. 6 (3), 325–333.
Ashoori, E., van der Heijden, T.L.M., Rossen, W.R., 2010. Fractional-flow theory of foam displacements with oil. SPE J. 15 (2), 260–273.
Azevedo, A.V., de Souza, A.J., Furtado, F., Marchesin, D., Plohr, B., 2010. The solution by the wave curve method of three-phase flow in virgin reservoirs. Transp. Porous Med. 83 (1), 99–125.
Bertin, H., Estrada, E.D.C., Atteia, O., 2017. Foam placement for soil remediation. Environ. Chem. 14 (5), 338–343.
Boeije, C.S., Rossen, W., 2015. Fitting foam-simulation-model parameters to data: I. coinjection of gas and liquid. SPE Reservoir Eval. Eng. 18 (2), 264–272.
Bui, M., Adjiman, C.S., Bardow, A., Anthony, E.J., Boston, A., Brown, S., et al., 2018. Carbon capture and storage (CCS): the way forward. Energy Environ. Sci. 11 (5), 1062–1176.
Castañeda, P., Abreu, E., Furtado, F., Marchesin, D., 2016. On a universal structure for immiscible three-phase flow in virgin reservoirs. Comput. Geosci. 20 (1), 171–185.
Castañeda, P., 2018. Explicit construction of effective flux functions for Riemann solutions. In: Klingenberg, C., Westdickenberg, M. (Eds.), Theory, Numerics and Applications of Hyperbolic Problems I, Presented at the XVI International Conference on Hyperbolic Problems: Theory, Numerics, Applications, vol. 236. Springer Proceedings in Mathematics & Statistics, pp. 273–284.
Castañeda, P., Marchesin, D., Furtado, F., 2022. Universality of Riemann solutions in porous media. Bol. Soc. Matemat. Mexic. 28, 1–21.
Castaneda-Herrera, C.A., Stevens, G.W., Haese, R.R., 2018. Review of CO_2 leakage mitigation and remediation technologies. Geological Carbon Storage: Subsurface Seals and Caprock Integrity 238, 327.
Charbeneau, R.J., 1988. Multicomponent exchange and subsurface solute transport: characteristics, coherence, and the Riemann problem. Water Resour. Res. 24 (1), 57–64.
Cheng, L., Reme, A.B., Shan, D., Coombe, D.A., Rossen, W.R., 2000. Simulating foam processes at high and low foam qualities. In: Presented at the SPE/DOE Improved Oil Recovery Symposium. Tulsa, Oklahoma, April 3-5, 2000.
Computer Modelling Group (Calgary, Alberta, Canada), STARS User's Guide, Version 2015. See also *GEM User's Guide*.
Cui, L., Ma, K., Puerto, M., Abdala, A.A., Tanakov, I., Lu, L.J., et al., 2016. Mobility of ethomeen C12 and carbon dioxide (CO_2) foam at high temperature/high salinity and in carbonate cores. SPE J. 21 (4), 1151–1163.
Dharma, A.S., 2013. Simulation Studies of Foam for Enhanced Oil Recovery. Delft University of Technology. MSc thesis. http://resolver.tudelft.nl/uuid:8276c89d-97ce-4d6f-a149-cdb04b71078c.
Estrada, E.D.C., Bertin, H., Atteia, O., 2015. Experimental study of foam flow in sand columns: surfactant choice and resistance factor measurement. Transp. Porous Med. 108 (2), 335–354.
Farajzadeh, R., Andrianov, A., Krastev, R., Hirasaki, G.J., Rossen, W.R., 2012. Foam–oil interaction in porous media: implications for foam assisted enhanced oil recovery. Adv. Colloid Interface Sci. 183–184, 1–13.
Furtado, F., 1991. Structural Stability of Nonlinear Waves for Conservation Laws. New York University. Ph.D. dissertation.
Glass, R.J., Yarrington, L., 2003. Mechanistic modeling of fingering, nonmonotonicity, fragmentation, and pulsation within gravity/buoyant destabilized two-phase/unsaturated flow. Water Resour. Res. 39 (3), 1058.
Khatib, Z.I., Hirasaki, G.J., Falls, A.H., 1988. Effects of capillary pressure on coalescence and phase mobilities in foams flowing through porous media. SPE Reserv. Eng. 3 (3), 919–926.
Kim, J.S., Dong, Y., Rossen, W.R., 2005. Steady-state flow behavior of CO_2 foam. SPE J. 10 (4), 405–415.
Kovscek, A.R., Patzek, T.W., Radke, C.J., 1995. A mechanistic population balance model for transient and steady-state foam flow in Boise sandstone. Chem. Eng. Sci. 50 (23), 3783–3799.
LaForce, T., Johns, R.T., 2005. Analytical solutions for surfactant-enhanced remediation of nonaqueous phase liquids. Water Resour. Res. 41 (10).
Lake, L.W., Johns, R.T., Rossen, W.R., Pope, G., 2014. Fundamentals of Enhanced Oil Recovery. Society of Petroleum Engineers, Richard, Texas.
Liu, T.P., 1974. The Riemann problem for general 2×2 conservation laws. Trans. Am. Math. Soc. 199, 89–112.
Liu, M., Andrianov, A., Rossen, W.R., 2011. Sweep efficiency in CO_2 foam simulations with oil. In: Presented at the IOR 2011 - 16th European Symposium on Improved Oil Recovery. Cambridge, UK, April 12-14, 2011.
Lyu, X., Voskov, D., Tang, J., Rossen, W.R., 2021. Simulation of foam enhanced-oil-recovery processes using operator-based linearization approach. SPE J. 26 (4), 2287–2304.
Osterloh, W.T., Jante Jr., M.J., 1992. Effects of gas and liquid velocity on steady-state foam flow at high temperature. In: Presented at the SPE/DOE Enhanced Oil Recovery Symposium. Tulsa, Oklahoma, April 22-24, 1992.
Reynolds, C., Krevor, S., 2015. Characterizing flow behavior for gas injection: relative permeability of CO_2-brine and N_2-water in heterogeneous rocks. Water Resour. Res. 51 (12), 9464–9489.
Rossen, W.R., 1996. Foams in enhanced oil recovery. In: Foams: Theory, Measurements, and Applications. MaRcel Dekker, pp. 413–464.
Rossen, W.R., 2013. Numerical challenges in foam simulation: a review. In: Presented at the SPE Annual Technical Conference and Exhibition. New Orleans, Louisiana, USA, September 30 - October 2, 2013.
Rossen, W.R., Venkatraman, A., Johns, R.T., Kibodeaux, K.R., Lai, H., Tehrani, N.M., 2011. Fractional flow theory applicable to Non-Newtonian behavior in EOR processes. Transp. Porous Med. 89 (2), 213–236.
Rossen, W.R., Farajzadeh, R., Hirasaki, G.J., Amirmoshiri, M., 2024. Potential and challenges of foam-assisted CO_2 sequestration. Geoenergy Sci. Eng. 239, 212929.
Schramm, L.L., 1994. In: Joan, Comstock M. (Ed.), Foams: Fundamentals and Applications in the Petroleum Industry, vol. 242. American Chemical Society, pp. i–vii.
Tang, J., Vincent-Bonnieu, S., Rossen, W.R., 2019a. Experimental investigation of the effect of oil on steady-state foam flow in porous media. SPE J. 24 (1), 140–157.
Tang, J., Ansari, M.N., Rossen, W.R., 2019b. Quantitative modeling of the effect of oil on foam for enhanced oil recovery. SPE J. 24 (3), 1057–1075.
Tang, J., Castañeda, P., Marchesin, D., Rossen, W.R., 2019c. Three-phase fractional-flow theory of foam-oil displacement in porous media with multiple steady states. Water Resour. Res. 55 (12), 10319–10339.
Tang, J., Castaneda, P., Marchesin, D., Rossen, W.R., 2022. Foam-oil displacements in porous media: insights from three-phase fractional-flow theory. In: Presented at 2022 Abu Dhabi International Petroleum Exhibition and Conference. SPE, in Abu Dhabi, UAE, D042S195R003.
Tang, J., Wei, B., Yang, M., Rossen, W.R., 2025. Critical thresholds for CO_2 foam generation in homogeneous porous media. SPE J. 30 (1), 439–454.
Thompson, K., Gdanski, R.D., 1993. Laboratory Study Provides guidelines for diverting acid with foam. SPE Production & Facilites 8 (4), 285–290.
Wu, Q., Ding, L., Zhao, L., Alhashboul, A.A., Almajid, M.M., Patil, P., et al., 2024. CO_2 soluble surfactants for carbon storage in carbonate saline aquifers with achievable injectivity: implications from the continuous CO_2 injection study. Energy 290, 130064.
You, K., DiCarlo, D., Flemings, P.B., 2015. Quantifying hydrate solidification front advancing using method of characteristics. J. Geophys. Res. Solid Earth 120 (10), 6681–6697.
Yu, G., Rossen, W.R., 2022. Simulation models for the minimum velocity for foam generation and propagation. J. Petrol. Sci. Eng. 214, 110406.
Zhou, Z., Rossen, W.R., 1995. Applying fractional-flow theory to foam processes at the "limiting capillary pressure.". SPE Adv. Technol. 3 (1), 154–162.